Dual boundary element method for analyzing three-dimensional cracks in layered and graded halfspaces

Sha Xiao[a], Zhongqi Quentin Yue[a*], Hongtian Xiao[b]

[a] Department of Civil Engineering, The University of Hong Kong, Hong Kong, PR China

[b] College of Civil Engineering and Architecture, Shandong University of Science and Technology, Qingdao, PR China

Abstract

This paper presents a dual boundary element analysis of three-dimensional cracks in layered and graded halfspaces. The fundamental solution of a multilayered solid is used to develop the dual boundary element method so that only the external boundary surface and crack surface need to be discretized while the material interfaces do not need to be discretized. Infinite boundary elements and crack-tip discontinuous elements are introduced to consider the far-fields of a layered halfspace and capture the crack-tip behavior, respectively. Special attentions are given to strongly singular and hypersingular integrals in the discretized displacement and traction boundary integral equations. For square-shaped, penny-shaped and elliptical cracks located in a homogeneous halfspace, the stress intensity factors obtained with the present formulation are in very good agreement with existing numerical results and closed-form solutions. The square-shaped cracks in horizontally layered halfspaces and the penny-shaped and elliptical cracks in graded halfspaces are analyzed. Results show that the material heterogeneity in layered and graded halfspaces can have a profound effect on the stress intensity factors.

Keywords: layered and graded halfspaces, dual boundary element method, fracture mechanics, stress intensity factors, infinite elements, discontinuous elements

[*] Corresponding Author: Z. Q. Yue, Email: yueqzq@hku.hk, Tel: +852-28591967

1. Introduction

1.1 Background

Layered materials, such as sedimentary rocks and layered crystals, widely exist in nature or man-made structures. It has been well recognized that non-homogeneity of layered solids has a significant effect on the deformation and failure in crack free or cracked solids. The problems of fracture in layered solids are extremely important and have been studied in depth. Many analytical and numerical methods can be used to analyze fracture mechanics problems in layered solids. Arin and Erdogan [1] analyzed a penny-shaped crack in an elastic layered solid by solving integral equations. Lin and Keer [2] calculated the crack opening displacements for a vertical planar crack in a layered transversely isotropic medium by the boundary integral equation method. Kuo and Keer [3] and Noda et al. [4] used the body force method to investigate penny-shaped and elliptical cracks in multilayered composites, respectively. Zhang and Jeffrey [5] studied crack problems in three-layered elastic media using an image method. Alaimo et al. [6] and Xiao and Yue [7] applied boundary element methods to layered composite structures.

Functionally graded materials (FGMs), which appeared in 1984, are another type of composite materials formed of two or more constituent phases with a continuously variable composition. Owing to their unique combination of mechanical and physical properties, FGMs have been chosen for advanced engineering applications. The mechanical responses of FGMs are especially important in many engineering fields and are of great interest to material scientists, design and manufacturing engineers. Jin and Noda [8], Ozturk and Erdogan [9], Paulino [10], Yue et al. [11], etc., analyzed the fracture mechanics in FGMs. Birman and Byrd [12] further reviewed the principal developments in various aspects of theories and applications of FGMs, including the problems of fracture and fatigue of FGMs.

In linear elastic fracture mechanics, the stress intensity factors (SIFs) play a major role in the description of singular stress fields and the prediction of crack propagations. For some simple geometrical and loading conditions of cracked bodies, the SIFs can be found from handbooks (e.g., Rooke and Cartwright [13]; Tada et al. [14]). It should be mentioned that Rooke and his

co-workers have used compounding methods [15, 16], integral transforms [17] and weight functions [18] to analyze different types of two- and three-dimensional crack problems and calculate SIFs. For complicated boundary conditions of layered and cracked bodies, the numerical methods must be developed for obtaining SIFs and other fracture parameters.

1.2 Literature review of boundary element methods

The boundary element method (BEM) is now firmly established in many engineering disciplines and is increasingly observed as an effective and accurate numerical approach (Cheng and Cheng [19]). The attraction of BEM can largely be attributed to the reduction in the dimensionality of the problem and to the efficient modeling of the stress concentration. Fracture mechanics has been the most active specialized area of research using BEM (for review and references see Aliabadi [20]). Since the geometric coincidence of opposite nodes across the crack surface provides identical equations for these nodal points, straightforward application of the conventional BEM to crack problems leads to a mathematical degeneration. To overcome this difficulty, the multi-domain technique of the BEM, which needs to introduce artificial boundaries into the cracked body, has been suggested. However, this method is not efficient because artificial boundaries results in the increase of the numbers of algebraic equations and boundary elements.

Hong and Chen [21] developed dual boundary integral equations for problems containing degenerate boundaries and Chen and Hong [22] presented the advances of dual boundary element methods (DBEM) with emphasis on hypersingular integrals and divergent series. The DBEM for analysis of fracture mechanics have two sets of boundary integral equations: displacement boundary integral equation and traction boundary integral equation. In the conventional DBEM, the displacement boundary integral equation is collocated on the external boundary surface and on one side of crack surface while the traction boundary integral equation is collocated on the other side of the crack surface. This DBEM was firstly developed by Portela et al. [23] for two-dimensional problems and then extended to three-dimensional problems by Mi and Aliabadi [24]. Portela et al. [25] and Mi and Aliabadi [26] further used the DBEM for analysis of crack growth. Aliabadi [20] reviewed the development of DBEMs in the analysis of

the fracture mechanics. More recently, Aliabadi and his co-workers (e.g., Wen and Aliabadi [27]; Li et al. [28]) investigated different types of fracture problems using DBEMs.

In applying the conventional DBEM, the displacements on either side of the crack surface are collocated as unknown variables. However, the displacements may be unnecessary for the calculation of SIFs and increase the calculation amounts. Pan and Amaidei [29] and Pan [30] developed another type of DBEM for two-dimensional anisotropic cracked solids, which applies the displacement integral equation to the external boundary surface only and the traction integral equation on one side of the crack surface. Pan and Yuan [31] further developed this DBEM for the analysis of three-dimensional cracks in anisotropic solids and described its advantages in detail. Using this single-domain BEM, many researchers have studied different types of crack problems. Cisilino et al. [32,33] investigated linear and nonlinear crack growth using the DBEM. Yue et al. [34] and Xiao and Yue [7] incorporated the fundamental solutions of transversely isotropic bi-materials and multi-layered isotropic solids into this DBEM for the analysis of three-dimensional crack problems in two different materials. Dong et al. [35] extended the DBEM for the analysis of cracked transversely isotropic and inhomogeneous solids. Herein, we will further develop this single-domain BEM for the study of three-dimensional cracks in horizontally layered and graded halfspaces.

1.4 Aim and approach of this study

The layered and graded solids containing cracks can be assumed as cracked halfspaces. In this paper, we will present a numerical implementation of the DBEM for the analysis of three-dimensional cracks, shown in Figs. 1 and 2. The generalized Kelvin solutions in a multilayered fullspace proposed by Yue [36] are applied as the fundamental solution in DBEM. As a result, only the external boundary surface and crack surface need to be discretized while the material interfaces do not need to be discretized. Furthermore, two types of boundary elements and three types of nine-node crack elements are used to discretize the external boundary surface and the crack surface, respectively. Special attentions are given to various singular integrals involved in the discretized boundary and traction integral equations. Finally, the proposed DBEM is applied to solve several crack problems in layered and graded halfspaces. Compressive tractions

on the external boundary surface may induce closure over a part of the crack and opening over the exterior region (Selvadurai [37]). This will result in a unilateral contact problem of the Signorini-type where the magnitude of the zone contact needs to be determined. In this study, we shall only consider the cases of the crack opening under the action of loadings on the external boundary surface and the crack surface. The influence of crack positions and material properties in layered and graded halfspaces on stress intensity factors are analyzed in detail.

2. Dual boundary integral equations for a cracked and layered halfspace

2.1 General

The fundamental solution of a multilayered solid developed by Yue [36] is the analytical solution for the elastostatic field in a layered solid of infinite extent due to the action of concentrated point loads. More details of the solutions can be found in Yue [38,39]. The dissimilar homogeneous layers adhere an elastic solid of upper semi-infinite extent and another elastic solid of lower semi-infinite extent. As shown in Fig. 1, the interface between any two connected dissimilar layers is fully bonded and the layer number is an arbitrary non-negative integer. Since 2000, Yue and his co-workers (Xiao and Yue [40]) have incorporated this fundamental solution into the BEMs for the analysis of the fracture mechanics in layered solids and found the solutions for many specific problems of interests in science and technology.

As shown in Fig. 3, the boundaries of a cracked and layered halfspace can be divided into external boundary surface S at z=0 and the two sides of the crack surface Γ^+ and Γ^-. The boundary surface S is further divided into two parts S_F and S_I, which represent a core region around the traction area or near the crack surface and a far-field region beyond the traction area or the crack surface, respectively.

Following the procedure of Yue et al. [34] and Xiao et al. [41], the dual boundary integral equations for a cracked and layered halfspace can be easily introduced using the fundamental solution of a multilayered fullspace.

2.2 Displacement boundary integral equation

The displacement boundary integral equation (BIE) for a cracked and layered halfspace can be expressed as

$$\begin{aligned} c_{ij}\left(P_S\right)u_j\left(P_S\right)+\int_{S_F+S_I} t_{ij}^{Y}\left(P_S,Q\right)u_j\left(Q\right)dS\left(Q\right)+\int_{\Gamma^+} t_{ij}^{Y}\left(P_S,Q\right)\Delta u_j\left(Q\right)d\Gamma\left(Q\right) \\ =\int_{S_F+S_I} u_{ij}^{Y}\left(P_S,Q\right)t_j\left(Q\right)dS\left(Q\right) \end{aligned} \tag{1}$$

where P_S is a source point on the external boundary surface S (=S_F +S_I), Q is a field point on external boundary surface and/or crack surface, $t_{ij}^{Y}(P_S,Q)$ and $u_{ij}^{Y}(P_S,Q)$ are the kernel functions of the fundamental solution (see Appendix A), $t_j(Q)$ and $u_j(Q)$ are the tractions and displacements of the field point Q on the boundaries, $\Delta u_j(Q)$ is relative crack discontinuous displacements, $c_{ij}\left(P_S\right)$ is a coefficient that is dependent on the local boundary geometry at the source point P_S. For smooth boundaries, the free terms $c_{ij}\left(P_S\right)=0.5\delta_{ij}$.

2.3 Traction boundary integral equation

The traction boundary integral equation (BIE) for a cracked and layered halfspace can be expressed as

$$\begin{aligned} t_j\left(P_{\Gamma^+}\right)+n_i\left(P_{\Gamma^+}\right)\int_{S_F+S_I} T_{ijk}^{Y}\left(P_{\Gamma^+},Q\right)u_k\left(Q\right)dS\left(Q\right)+n_i\left(P_{\Gamma^+}\right)\int_{\Gamma^+} T_{ijk}^{Y}\left(P_{\Gamma^+},Q\right)\Delta u_k\left(Q\right)d\Gamma\left(Q\right) \\ =n_i\left(P_{\Gamma^+}\right)\int_{S_F+S_I} U_{ijk}^{Y}\left(P_{\Gamma^+},Q\right)t_k\left(Q\right)dS\left(Q\right) \end{aligned} \tag{2}$$

where P_{Γ^+} is a source point on the crack surface Γ^+, Q is a field point on external boundary surface and/or crack surface, respectively, $n_i\left(P_{\Gamma^+}\right)$ is the outward unit normal on the source point P_{Γ^+}, $T_{ijk}^{Y}\left(P_{\Gamma^+},Q\right)$ and $U_{ijk}^{Y}\left(P_{\Gamma^+},Q\right)$ are the new kernel functions of the fundamental solution obtained using the kernel functions $t_{ij}^{Y}\left(P_{\Gamma^+},Q\right)$ and $u_{ij}^{Y}\left(P_{\Gamma^+},Q\right)$ of the fundamental solution, which are presented in Xiao et al. [41].

3. Numerical scheme

Xiao et al. [41] and Yue et al. [34] presented the discretization techniques of the external boundary surface and the crack surface in detail, respectively. Details will not be presented here. Basically, the eight-node isoparametric elements are used to discretize the core region S_F and infinite boundary elements are used to discretize the far-field region S_I. Three types of continuous and discontinuous nine-node elements are introduced to discretize the crack surface. Continuous elements are used to discretize the crack surface far away from the crack tip and discontinuous elements are used to discretize the crack surface near the crack tip.

The coordinates at any point in a nine-node element are related to its element nodal coordinates as follows:

$$x=\sum_{\alpha=1}^{9}N_{\alpha}^{c}x^{\alpha}\ ,\quad y=\sum_{\alpha=1}^{9}N_{\alpha}^{c}y^{\alpha}\ ,\quad z=\sum_{\alpha=1}^{9}N_{\alpha}^{c}z^{\alpha} \tag{3a}$$

where N_{α}^{c} (α=1-9) are the shape functions of the elements on the crack surface. Detailed expressions for N_{α}^{c} (α=1-9) can be found in Yue et al. [34]. The nodes near the crack tip in discontinuous elements are at a distance of 1/3 from the element edge ξ=-1 or η=-1.

For the element on the crack surface, the discontinuous displacements are approximated by their nodal values

$$\Delta u_i=\sum_{\alpha=1}^{9}gN_{\alpha}^{c}\Delta u_i^{\alpha} \tag{3b}$$

where g is the coefficient for capturing the characteristics of the discontinuous displacements near the crack front and is presented by

(1) $g=1$ for the continuous element,

(2) $g=\sqrt{1+\eta}$ for the discontinuous element type I, and

(3) $g=\sqrt{(1+\xi)(1+\eta)}$ for the discontinuous element type II.

Suppose that the crack front is smooth and the crack front is away from the material interface.

The stress and displacement near the crack front, respectively, vary with $1/\sqrt{r}$ and $\sqrt{r}$, where *r* is as defined in Fig. 4. The relation of the discontinuous displacements on the crack surface and the SIFs can be expressed as

$$K_{\mathrm{I}} = \frac{E}{4\left(1-\nu^2\right)}\sqrt{\frac{\pi}{2r}}\Delta u_3\left(r,\theta=-\frac{\pi}{2},\frac{3\pi}{2},\varphi=\frac{\pi}{2}\right) \tag{4a}$$

$$K_{\mathrm{II}} = \frac{E}{4\left(1-\nu^2\right)}\sqrt{\frac{\pi}{2r}}\Delta u_2\left(r,\theta=-\frac{\pi}{2},\frac{3\pi}{2},\varphi=\frac{\pi}{2}\right) \tag{4b}$$

$$K_{\mathrm{III}} = \frac{E}{4\left(1+\nu\right)}\sqrt{\frac{\pi}{2r}}\Delta u_1\left(r,\theta=-\frac{\pi}{2},\frac{3\pi}{2},\varphi=\frac{\pi}{2}\right) \tag{4c}$$

where (x_1, x_2, x_3) and (r, θ, φ) are, respectively, the Cartesian coordinate and spherical coordinate systems located at the crack front.

The discontinuous displacements near the crack front can be used to obtain accurate SIF values. Here, the discontinuous displacements at the points $\left(\xi,\eta\right)=\left(-1+10^{-5},\eta\right)$ or $\left(\xi,\eta\right)=\left(\xi,-1+10^{-5}\right)$ of a discontinuous element near the crack front are calculated by using Eq. (3b) and are substituted into Eq. (4) to obtain SIF values.

4. Numerical integration

4.1 General

In the displacement BIE (1), the source point *PS* is positioned on the external boundary surface, i.e., the horizontal boundary surface. In this case, on the left-hand side of Eq. (1), there are strongly singular integrals and on the right-hand side of Eq. (1), there are weakly singular integrals. In the traction BIE (2), the source point P_{Γ^+} is positioned on the crack surface. All the integrals on the external boundary surface in Eq. (2) are not singular. On the right-hand side of Eq. (2), there are hypersingular integrals.

The regular integrals in Eqs. (1) and (2) can be calculated by using Gaussian quadrature. The weakly singular integrals in Eq. (1) are computed by applying an integration scheme based on a linear coordinate transformation (Beer [42]). In the ensuing, the evaluation of the strongly singular integrals in Eq. (1) and the hypersingular integral in Eq. (2) will be introduced.

4.2 Strongly singular and hypersingular integrals

In the formulations of the dual boundary element methods by Pan et al. [31] and Yue et al. [34], the strongly singular integrals together with the free term c_{ij} can be evaluated by the rigid-body motion method. However, because of using infinite boundary elements in Eq. (1), this indirect method cannot be used for the analysis of the strongly singular integrals. In this case, the strongly singular integrals and the free term c_{ij} need to be calculated directly. Pan and Yuan [31] proposed the numerical method for the evaluation of the hypersingular integrals in the traction BIE (2). Herein, we use the methods proposed by Pan and Yuan [31] for developing numerical quadrature methods for strongly singular and hypersingular integrals in Eqs. (1) and (2). The proposed method applies Kutt's numerical quadrature (Kutt [43,44]).

On the isoparametric and infinite boundary elements of the external boundary surface in Eq. (1), the strongly singular integrals can be expressed as

$$\int_{-1}^{1}\int_{-1}^{1} t_{ij}^{Y}\left[P_S\left(\xi^c,\eta^c\right),Q\left(\xi,\eta\right)\right]N_\alpha\left(\xi,\eta\right)J\left(\xi,\eta\right)d\xi d\eta \tag{5a}$$

$$\int_{-1}^{1}\int_{-1}^{1} t_{ij}^{Y}\left[P_S\left(\xi^c,\eta^c\right),Q\left(\xi,\eta\right)\right]{}^{\infty}N_\alpha^u\left(\xi,\eta\right)J\left(\xi,\eta\right)d\xi d\eta \tag{5b}$$

where N_α and ${}^{\infty}N_\alpha^u$ are, respectively the interpolation functions of isoparametric and infinite boundary elements, J is the Jacobian transformation and the collocation point $P_S\left(\xi^c,\eta^c\right)$ coincides with one of the nodal points on the element. It can be observed that the integrand is $O\left(r^{-2}\right)$.

On the elements of the crack surface in Eq. (2), the hypersingular integrals can be expressed as

$$\int_{-1}^{1}\int_{-1}^{1} T_{ijk}^{Y}\left[P_{\Gamma^+}\left(\xi^c,\eta^c\right),Q\left(\xi,\eta\right)\right]g\left(\xi,\eta\right)N_\alpha^c\left(\xi,\eta\right)J\left(\xi,\eta\right)d\xi d\eta \tag{6}$$

where J is the Jacobian transformation and the collocation point $P_{\Gamma^+}\left(\xi^c,\eta^c\right)$ coincides with one of the nodal points on the element. It can be observed that the integrand is $O\left(r^{-3}\right)$.

Introducing the following polar coordinates transform

$$\begin{aligned}\xi &= \xi^c + r\cos\theta \\ \eta &= \eta^c + r\sin\theta\end{aligned} \tag{7}$$

Eqs. (5) and (6) can then be rewritten as

$$\sum_m \int_{\theta_1}^{\theta_2}\int_0^{R(\theta)} t_{ij}^Y\left[P_S\left(\xi^c,\eta^c\right),Q\left(r,\theta\right)\right]N_\alpha\left(r,\theta\right)J\left(r,\theta\right)rdrd\theta \tag{8a}$$

$$\sum_m \int_{\theta_1}^{\theta_2}\int_0^{R(\theta)} t_{ij}^Y\left[P_S\left(\xi^c,\eta^c\right),Q\left(r,\theta\right)\right]{}^{\infty}N_\alpha^t\left(r,\theta\right)J\left(r,\theta\right)rdrd\theta \tag{8b}$$

and

$$\sum_m \int_{\theta_1}^{\theta_2}\int_0^{R(\theta)} T_{ijk}^Y\left[P_{\Gamma^+}\left(\xi^c,\eta^c\right),Q\left(r,\theta\right)\right]g\left(r,\theta\right)N_\alpha^c\left(r,\theta\right)J\left(r,\theta\right)rdrd\theta \tag{9}$$

where the summation over m is for all the triangles on the element.

Now it can be observed that the integrands in Eq. (8) are of singularity $O\left(r^{-1}\right)$ and the integrand in Eq. (9) is of singularity $O\left(r^{-2}\right)$. Kutt's numerical quadrature can be utilized to evaluate the inner finite-part integral with respect to r. On the other hand, the outer integral with respect to θ is regular and can be calculated by the regular Gaussian quadrature.

For a given Gaussian quadrature θ_s, the inner integral in Eq. (8) can be approximated as N-equispace quadrature as follows

$$\int_0^R \frac{f\left(r\right)}{r}dr \approx \sum_{l=1}^{N}\left(w_l + c_l\, ln\, R\right)f\left(\frac{l-1}{N}R\right) \tag{10}$$

where w_l are the weights and c_l the coefficients given by Kutt, the integrand for the isoparametric element is given by

$$f\left(r\right) = t_{ij}^Y\left[P_S\left(\xi^c,\eta^c\right),Q\left(r,\theta_s\right)\right]N_\alpha\left(r,\theta_s\right)J\left(r,\theta_s\right)r^2 \tag{11a}$$

and the integrand for the infinite boundary element is given by

$$f(r)=t_{ij}^{Y}\left[P_S\left(\xi^c,\eta^c\right),Q\left(r,\theta_s\right)\right]^{\infty}N_{\alpha}^{u}\left(r,\theta_s\right)J\left(r,\theta_s\right)r^2 \tag{11b}$$

For a given Gaussian quadrature θ_s, the inner integral in Eq. (9) can be approximated as *N*-equispace quadrature as follows

$$\int_0^R\frac{f(r)}{r^2}dr\approx\frac{1}{R}\sum_{l=1}^{N}\left(w_l+c_l\,ln\,R\right)f\left(\frac{l-1}{N}R\right) \tag{12}$$

where w_l are the weights and c_l the coefficients given by Kutt, the integrand for the isoparametric boundary element is given by

$$f(r)=T_{ijk}^{Y}\left[P_{\Gamma^+}\left(\xi^c,\eta^c\right),Q\left(r,\theta_s\right)\right]g\left(r,\theta_s\right)N_{\alpha}\left(r,\theta_s\right)J\left(r,\theta_s\right)r^3 \tag{13}$$

It is point out that the weights w_l and the coefficients c_l in Eqs. (10) and (12) have different values for a given *l* value.

5. Numerical results and discussion

Based on the solution expressions presented above, the computer program has been written in FORTRAN to calculate the discontinuous displacements across crack surfaces and the displacements on the external boundary surface and further obtain the SIFs using the discontinuous displacements. In this section, several numerical examples including layered and graded solids are presented to verify the program and to show the efficiency and accuracy of the present DBEM formulation in calculating the SIFs. Numerical results also show that the material heterogeneity can have a profound effect on the SIFs.

5.1 A square-shaped crack in a homogenous halfspace

The first example given below is to analyze a square-shaped crack in a homogeneous halfspace, shown in Fig. 5. The square-shaped crack surfaces are parallel to the boundary surface z=0 and subjected to a uniform compressive stress p_0. The side length of the square is 2a. As shown in Fig. 3, the core region S_F of the traction free boundary is represented by a square area (5$a\times$5a). The center of the square core region S_F is identical to the origin of the coordinate system *Oxyz*.

The discretization mesh of the traction free boundary is shown in Fig. 6. The core region S_F is discretized with a total of 320 isoparametric elements. The far-field region S_I outside the square core region is discretized with a total of 64 infinite elements. The mesh of the crack surface is shown in Fig. 7. One hundred (10×10) nine-node elements are used to discretize the crack surface. Among these elements, there are 64 nine-node isoparametric elements, 32 discontinuous elements of type I, and four discontinuous elements of type II.

For the given loading and geometrical conditions, there are the same SIF values along the crack front of four sides of the square-shaped crack. Fig. 8 presents the variations of the normalized SIFs $KI = K_{\mathrm{I}} / \left(p_0 \sqrt{\pi a} \right), KII = K_{\mathrm{II}} / \left(p_0 \sqrt{\pi a} \right), KIII = K_{\mathrm{III}} / \left(p_0 \sqrt{\pi a} \right)$ along the crack front of one side of the square-shaped crack in a homogeneous halfspace with the depth d. It can be found that with the depth d increasing, the absolute SIF values of modes I, II and III decrease. At the depth d/a=6, the maximum SIF values KI=0.7580, KII=0.0008 and $KIII$=0.0009.

It is known that in the case of a square-shaped crack in a homogeneous fullspace, the variation of mode-I SIFs along the crack front is independent of the material properties and the SIF values of modes II and III are equal to zero. Pan and Yuan [31] and Weaver [45] respectively obtained the maximum mode-I SIF values of a square-shaped crack subject to a uniform compressive stress, i.e., KI=0.7626 and 0.74. It can be found that with the depth increasing, the SIF values of a square-shaped crack in a homogeneous halfspace approach the ones in a homogeneous fullspace and at d/a=6 the difference of the SIF values between two cases becomes negligible.

We choose two distances 1/4 and 1/3 of the nodes to the element edge ξ=-1 or η=-1 to analyze the influence of the positions of the nodes in discontinuous elements on the SIF. For a square-shaped crack in a homogeneous fullspace and subject to a uniform compressive stress, the maximum SIF values KI=0.7620 and 0.7626, respectively, for the distances 1/4 and 1/3. Numerical verifications illustrate that the SIFs are insensitive to the locations of these nodes in discontinuous elements.

5.2 Square-shaped cracks in layered bi-material halfspaces

5.2.1 General

The second example considers a square-shaped crack (the side length 2*a*) in a linear elastic halfspace composed of one layer bonded to another homogeneous halfspace, shown in Fig. 9. The square-shaped crack surfaces are parallel to the external boundary surface and the material interface. The layer and the halfspace are assigned the name: material 1, material 2 respectively. The coordinate systems (x,y,z) and (x',y',z') lie in the external boundary surface and the crack surface, respectively. The origin of the coordinate system (x',y',z') is situated at the center of the square-shaped crack, i.e., $(x,y,z)=(0,0,h)$. The thickness of the layer is designed 2*h* and the crack is located at *z*=*h*. The external boundary surface is discretized into the mesh shown in Fig. 6 and the crack surface is discretized into the mesh shown in Fig. 7. Two cases are considered as follows: Case 1: $E_1=20$ GPa, $\nu_1=0.3$ and $E_2=40$ GPa, $\nu_2=0.25$; Case 2: $E_1=40$ GPa, $\nu_1=0.25$ and $E_2=20$ GPa, $\nu_2=0.3$. In the ensuing, two different modes of loading are considered to illustrate the variations of the SIFs with material properties and crack positions.

5.2.2 A square-shaped crack under a compressive stress on the crack surface

The first mode of loading is that the crack surface is subject to a uniform compressive stress p_0, shown in Fig. 9. Fig. 10 illustrates the variations of the normalized SIFs $KI=K_{\mathrm{I}}/\left(p_0\sqrt{\pi a}\right)$, $KII=K_{\mathrm{II}}/\left(p_0\sqrt{\pi a}\right)$ and $KIII=K_{\mathrm{III}}/\left(p_0\sqrt{\pi a}\right)$ with the depth *h*. Table 1 presents the maximum values of the normalized SIFs *KI*, *KII* and *KIII*. For the given loading and geometrical conditions, there are the same SIF values along the crack front of four sides of the square-shaped crack. Herein, only the SIFs along the crack front of one side of the square-shaped crack are presented.

In Fig. 10, it can be found that all the SIF values approach the ones in a homogeneous fullspace as *h* increases. This is because the external boundary surface exerts a weak influence on the crack opening and sliding as the *h* value increase. The crack opening is constrained by the stiffer

lower halfspace (Case 1) and the constraint becomes more pronounced as the depth h decreasing. This induces the decrease of the SIF *KI* with the depth h increasing, as shown in Fig. 10a. As a result, for a given h value, the SIF *KI* for Case 1 is smaller than the one for Case 2. In Fig. 10b, the values of the SIF *KII* decrease with the depth h increasing and approaches zero in a homogeneous halfspace. As the stiffer lower halfspace (Case 1) exists, the crack sliding become more obvious and larger values of the SIF *KII* appear. As a result, for a given h value, the values of the SIF *KII* for Case 1 are larger than the ones for Case 2. It can also be found in Fig. 10c that the variations of the SIF *KIII* for Cases 1 and 2 with the depth h are much similar to the ones of the SIF *KII*.

5.2.3 A square-shaped crack under a tensile stress on the boundary surface

The second mode of loading is that the external boundary surface ($2a\times2a$) at z=0 is subject to a uniform tensile stress p_0, shown in Fig. 11. The centers of the loading domain and the square-shaped crack are, respectively, located at the points (0,0,0) and (0,0,h) of the coordinate system *Oxyz*. Fig. 11 illustrates the variations of the SIFs *KI*, *KII* and *KIII* with the depth h. Table 2 presents the maximum SIF values of the SIFs *KI*, *KII* and *KIII*. For the given loading and geometrical conditions, there are the same SIF values along the crack front of four sides of the square-shaped crack.

In Fig. 12 and Table 2, it can be found that all the SIF values approach zero as h increases. In Fig. 12a, for a given h value, the values of the SIF *KI* for Case 2 are larger than the ones for Case 1. This is because the crack opening is constrained by the stiffer lower halfspace (Case 1) and the constraint becomes more pronounced as the depth h decreasing. However, in Fig. 12b, for a given h value, the values of the SIF *KII* for Case 2 are smaller than the ones for Case 1. In Fig. 12c, for a given h value, the values of the SIF *KIII* for Case 2 are smaller than the ones for Case 1. These variations of the SIF values are much related to the lower halfspace. The stiffer lower halfspace (Case 1) exists, the crack sliding become more obvious. Comparing to the crack problem studied in Section 5.2.2, the SIF values of the square-shaped cracks under the action of two different loadings have the same variations for Cases 1 and 2. It can further be found that under the same conditions, the SIF values of the crack under the action of a compressive

stress on the crack surface are larger than the ones under the action of a tensile stress on the external boundary surface.

5.3 Penny-shaped and elliptical cracks in graded halfspaces

5.3.1 General

The third example given below is to analyze penny-shaped and elliptical cracks in nonhomogeneous halfspaces, shown in Fig. 2. The halfspace consists of a homogeneous halfspace and a nonhomogeneous layer and two materials are fully bonded. The crack is located at the interface between the graded layer and the homogeneous halfspace. The previous results show that in problems involving practical materials the influence of the Poisson's ratio on the stress intensity factors is rather insignificant [9]. In this study, it is assumed that the Poisson's ratio of the composite medium is constant ($\nu_1=\nu_2=0.3$) and the elastic modulus has the form

$$E_2(z)=E_1e^{\alpha(h-z)},\quad \alpha=\frac{1}{h}ln\left(E_2(z=0)/E_1\right) \tag{14}$$

where h is the thickness of the graded layer and α is a material constant representing the material gradients.

For $0\le z/a\le h$, the graded layer is closely approximated by n bonded layers of elastic homogeneous media. Each layer has the thickness equal to h/n and elastic modulus equal to $E_2(z)$ at the lower depth of the layer. A homogeneous material bonded with the graded layer is considered as a semi-infinite domain. For all the layers, the Poisson's ratios are the same and equal to 0.3. Fig. 13 illustrates an approximation of the continuous depth variation of the elastic modulus by a large number of piece-wisely homogeneous layers. It can be observed from Fig. 13 that a close approximation of the elastic modulus variation can be obtained using a large number of n. The results presented by Yue et al. [15] show that when n=20, the accurate stress intensity factors can be obtained. In the following analysis, the layer discretization number n=50 is used to calculate the discontinuous displacements on the crack surface.

It has been shown that the crack-tip field singularities and angular distributions in graded materials are as the same as those in homogeneous elastic solids provided that the properties of the material are continuous and piecewise differentiable (see Jin and Noda [8], Ozturk and Erdogan [9]). The result is independent of the material properties and the orientation of the crack. Thus, Eq. (4) can be further used to calculate the SIF values of the cracks in a graded material.

5.3.2 A penny-shaped crack under a compressive stress on the crack surface

As shown in Fig. 2, a penny-shaped crack is located at the interface between a graded layer and a homogeneous halfspace. The crack surfaces are subject to a uniform compressive stress p_0 and the boundary surface at z=0 is not subject to any loadings. The boundary surface at z=0 is discretized into the mesh shown in Fig. 6 and the crack surface is discretized into the mesh shown in Fig. 14.

Fig. 15 illustrates the variations of the normalized SIFs *KI* and *KII* where $KI = K_{\mathrm{I}} / K_0$ and $KII = K_{\mathrm{II}} / K_0$ ($K_0 = 2p_0\sqrt{a/\pi}$). The corresponding SIF values are also listed in Table 3. For the given values of h and α, there are the same SIF values of modes I and II at any positions of the crack tip. For the penny-shaped crack (h/a=2) in a homogeneous halfspace, *KI*=1.06458 and *KII*=0.01414 from the present BEM as compared with *KI*=1.048 and *KII*=0.015 in Rooke and Cartwright [13]. In Fig. 15, the SIF values (*KI* and *KII*) for positive and negative α values are located below and above the SIF values curve for α=0, respectively. As the absolute α value increases, the SIF values monotonically move away from the SIF curve from α=0. Additionally, for a given α value, as the depth h increases the SIF values decrease. For $h/a \geq 1.8$, *KII* does not vary obviously with the depth h increasing. The above results indicate the following physical understandings. For the crack in a compliant body (i.e., $\alpha > 0$ or $E_1 < E_2$), the crack opening is constrained by the upper stiffer graded layer so that the SIF values decrease. On the other hand, for the crack in a stiffer solid (i.e., $\alpha < 0$ or $E_1 > E_2$), the SIF values gain enlarged.

5.3.3 An elliptical crack under a compressive stress on the crack surface

As shown in Figs. 2 and 16, an elliptical crack (a=2b) is located at the interface between a graded layer and a homogeneous halfspace. The crack surfaces are subject to a uniform compressive stress p_0 and the boundary surface at z=0 is not subject to any loadings. The boundary surface at z=0 is discretized into the mesh shown in Fig. 6 and the mesh of the crack surface is much similar to the one shown in Fig. 14.

Figs. 17-19 illustrate the variations of the normalized SIFs *KI*, *KII* and *KIII* where $KI = K_{\mathrm{I}} / \left(p_0 \sqrt{\pi b} \right)$, $KII = K_{\mathrm{II}} / \left(p_0 \sqrt{\pi b} \right)$ and $KIII = K_{\mathrm{III}} / \left(p_0 \sqrt{\pi b} \right)$. The mode I and II SIF values at the minor-axis crack tip are also listed in Table 4. The SIF values are presented as functions of the nonhomogeneous parameter α and the crack distance h from the boundary surface z=0. At the minor-axis crack tip (i.e., β=90°) of the elliptical crack in a homogeneous halfspace, for h/a=0.5 and 1, *KI*=1.18058 and 0.92462, respectively, from the present BEM as compared with *KI*=1.1878 and 0.91536 in Noda et al. [4].

Fig. 17 illustrates the variations of the mode I SIF values at the crack tip $\left(x', y', z' \right) = \left(a, 0, 0 \right)$ (i.e., β=0°) and $\left(0, b, 0 \right)$ (i.e., β=90°) with the parameters α and h. With β increasing from 0° to 90°, the mode I SIF values increase. It means that the mode I SIF has the maximum value at the minor-axis crack tip. It can be further found that the mode I SIF values for positive and negative values of α are located, respectively, at the two sides of the SIF curve for α=0. Note that the curve for α=0 presents the SIF values for the crack in a homogeneous halfspace. As the α values decrease, the mode I SIF values increase. This is because that more compliant for the graded layer, more easy the crack opening. For a given α value, the SIF values decrease with the depth h increasing and do not vary obviously after some depth.

Fig. 18 shows the variations of the mode II SIF values at the crack tip $\left(x', y', z' \right) = \left(a, 0, 0 \right)$ (i.e., β=0°) and $\left(0, b, 0 \right)$ (i.e., β=90°) with the parameters α and h. With β increasing

from 0° to 90°, the mode II SIF values increase. It means that the mode II SIF has the maximum value at the minor-axis crack tip. It can be found that the mode II SIF values for positive and negative values of α are located, respectively, at the two sides of the SIF curve for $\alpha=0$. As the α values decrease, the mode II SIF values increase.

Fig. 19 shows the variations of the mode III SIF values at the crack tips $\beta=39.64°, 63.43°$ with the parameters α and h. Table 5 presents the mode III SIF values at the crack tips $\beta=39.64°$, 63.43°. It is obvious that the absolute values of the mode III SIF at $\beta=63.43°$ is larger than the ones at $\beta=39.64°$. Because of symmetry, the mode III SIF values are equal to zero at the crack tips $\beta=0^{o}$ and 90°. It can be further found that the mode III SIF values for positive and negative values of α are located, respectively, at the two sides of the SIF curve for $\alpha=0$. As the α values decrease, the mode III SIF values increase.

5.3.4 Comparison of penny-shaped and elliptical cracks in graded halfspaces

To find the influence of the crack geometries on the SIFs, we compare the penny-shaped and elliptical cracks in graded halfspaces analyzed above. From the above results, one can have the following observations:

(1) Because of the crack geometry and the nonhomogeneous properties of the graded layer, the two modes of SIFs (I and II) of the penny-shaped crack are coupled together and the mode III SIF does not exist. However, for the elliptical crack in a graded halfspace, all the three modes of SIFs (I, II and III) exist and are coupled together.

(2) The penny-shaped crack in a graded halfspace has the same SIF values along all the crack tips. However, the elliptical crack in a graded halfspace has different SIF values for the crack tips with different β values ($0^{o} < \beta < 90^{o}$).

6. Conclusions

This paper develops a new DBEM for the efficient analysis and accurate calculation of the stress intensity factors of three-dimensional cracks in layered and graded solids. The application of the fundamental solution of a layered solid can eliminate the requirement of mesh discretization on material interfaces so that only the horizontal boundary surface and the crack surface need to be discretized. Different types of elements are utilized for the discretization of the boundary surface and the crack surface. The corresponding numerical schemes are introduced to the discretized boundary integral equations.

The calculation of the SIFs for three-dimensional cracks in layered and graded halfspaces is conducted. The SIF values obtained by the proposed DBEM are in very good agreement with the exiting numerical results and the effects of material properties and crack positions on the SIFs are demonstrated. More detailed investigations, such as cracks reaching and going through material interfaces or other cracks in graded solids, need to be carried out for accurately enhancing our knowledge for fracture mechanics in layered and graded solids. Some of the related problems are currently under investigation by the authors and results will be published in a separate paper.

Acknowledgements

The authors would like to thank the financial supports from the Research Grants Council of Hong Kong SAR Government (GRF Nos. 17204415 and 17207518) and the National Natural Science Foundation of China (Grant No. 41672291). The authors are grateful to the reviewers for their valuable comments and suggestions, which have greatly improved the manuscript presentation.

Appendix A

The fundamental solutions $t_{ij}^{Y}\left(P,Q\right)$ and $u_{ij}^{Y}\left(P,Q\right)$ for a multilayered elastic medium, shown in Eq. (1), may be expressed as

$$t_{ij}^{Y}\left(P,Q\right)=\sigma_{ik}\left(P,Q\right)\big|_{F_j=1}\,n_k\left(Q\right) \tag{A1}$$

$$u_{ij}^{Y}\left(P,Q\right)=u_i\left(P,Q\right)\big|_{F_j=1} \tag{A2}$$

where F_j is a concentrated force acted at the source point $P(0,0,h)$ along the *j* direction, $\sigma_{ik}(P,Q)\big|_{F_j=1}$ and $u_i(P,Q)\big|_{F_j=1}$ are, respectively, the stresses and displacements at the field source $Q(x,y,z)$ induced by the concentrated force F_j and $n_k(Q)$ is the outward normal component of the field point *Q*.

Yue [36, 38, 39] utilized classical integral transforms and a backward transfer matrix method to develop the closed-form fundamental solution of the stresses $\sigma_{ik}(P,Q)$ and displacements $u_i(P,Q)$ in Eqs. (A1) and (A2). For completeness, the essential formulations are presented in the ensuing.

For a layered medium, the vector fields of displacements, stresses and strains are defined as

$$\mathbf{u}=\begin{bmatrix} u_x & u_y & u_z \end{bmatrix}^{\mathbf{T}},\ \mathbf{T}_z=\begin{bmatrix} \sigma_{xz} & \sigma_{yz} & \sigma_{zz} \end{bmatrix}^{\mathbf{T}},\ \mathbf{\Gamma}_p=\begin{bmatrix} \varepsilon_{xx} & \varepsilon_{xy} & \varepsilon_{yy} \end{bmatrix}^{\mathbf{T}} \tag{A3}$$

where the superscript T stands for the transpose of a matrix and the symbol (P,Q) is omitted for simplification.

For concentrated point loads, i.e., $\mathbf{F}_c=\begin{bmatrix} F_x & F_y & F_z \end{bmatrix}^{\mathbf{T}}$, the solution expressions of the layer medium are presented as follows

$$\mathbf{u}=\mathbf{G}_u\mathbf{F}_c,\ \mathbf{T}_z=\mathbf{G}_z\mathbf{F}_c,\ \mathbf{\Gamma}_p=\mathbf{G}_p\mathbf{F}_c \tag{A4}$$

where the matrices $\mathbf{G}_u$, $\mathbf{G}_z$ and $\mathbf{G}_p$ can be expressed as

$$2\pi\mathbf{G}_u(x,y,z)=\int_0^\infty \begin{pmatrix} \Phi_1 J_0-\dfrac{x^2-y^2}{r^2}\Phi_2 J_2 & -\dfrac{2xy}{r^2}\Phi_2 J_2 & -\dfrac{x}{r}\Phi_{13}J_1 \\ -\dfrac{2xy}{r^2}\Phi_2 J_2 & \Phi_1 J_0+\dfrac{x^2-y^2}{r^2}\Phi_2 J_2 & -\dfrac{y}{r}\Phi_{13}J_1 \\ \dfrac{x}{r}\Phi_{31}J_1 & \dfrac{y}{r}\Phi_{31}J_1 & \Phi_{33}J_0 \end{pmatrix} d\rho \tag{A5}$$

$$2\pi\mathbf{G}_z(x,y,z)=\int_0^\infty\begin{pmatrix}\Psi_1J_0-\frac{x^2-y^2}{r^2}\Psi_2J_2 & -\frac{2xy}{r^2}\Psi_2J_2 & -\frac{x}{r}\Psi_{13}J_1\\ -\frac{2xy}{r^2}\Psi_2J_2 & \Psi_1J_0+\frac{x^2-y^2}{r^2}\Psi_2J_2 & -\frac{y}{r}\Psi_{13}J_1\\ \frac{x}{r}\Psi_{31}J_1 & \frac{y}{r}\Psi_{31}J_1 & \Psi_{33}J_0\end{pmatrix}d\rho \tag{A6}$$

$$\begin{aligned}2\pi\mathbf{G}_p(x,y,z)=&-\frac{1}{2}\int_0^\infty\begin{pmatrix}\frac{x}{r}(2\Phi_1+\Phi_2)J_1 & \frac{y}{r}\Phi_2J_1 & \Phi_{13}J_0\\ \frac{y}{r}\Phi_1J_1 & \frac{x}{r}\Phi_1J_1 & 0\\ \frac{x}{r}\Phi_2J_1 & \frac{y}{r}(2\Phi_1+\Phi_2)J_1 & \Phi_{13}J_0\end{pmatrix}\rho d\rho\\ &+\frac{1}{2}\int_0^\infty\begin{pmatrix}\left(\frac{4x^2}{r^3}-\frac{3x}{r}\right)\Phi_2J_3 & \left(\frac{3y}{r}-\frac{4y^3}{r^3}\right)\Phi_2J_3 & \frac{x^2-y^2}{r^2}\Phi_{13}J_2\\ \left(\frac{3y}{r}-\frac{4y^3}{r^3}\right)\Phi_2J_3 & \left(\frac{3x}{r}-\frac{4x^3}{r^3}\right)\Phi_2J_3 & \frac{2xy}{r^2}\Phi_{13}J_2\\ \left(\frac{3x}{r}-\frac{4x^3}{r^3}\right)\Phi_2J_3 & \left(\frac{4y^3}{r^3}-\frac{3y}{r}\right)\Phi_2J_3 & \frac{y^2-x^2}{r^2}\Phi_{13}J_2\end{pmatrix}\rho d\rho\end{aligned} \tag{A7}$$

where $r=\sqrt{x^2+y^2}$, $\Phi_1=\frac{1}{2}\left[\Phi_{11}+\Phi_{22}\right]$, $\Phi_2=\frac{1}{2}\left[\Phi_{11}-\Phi_{22}\right]$, $\Psi_1=\frac{1}{2}\left[\Psi_{11}+\Psi_{22}\right]$ and $\Psi_2=\frac{1}{2}\left[\Psi_{11}-\Psi_{22}\right]$. The following identity of Bessel functions (J_m) of order *m* is used in the further reduction

$$\frac{1}{2\pi}\int_0^{2\pi}e^{\pm i(\rho r\sin\Psi-m\Psi)}d\psi=J_m(\rho r)=J_m\quad m=0,\pm1,\pm2,\cdots \tag{A8}$$

The expressions of the matrices $\mathbf{G}_u$, $\mathbf{G}_z$ and $\mathbf{G}_p$ include the inverse Hankel transform integrals with a semi-infinite interval. The expressions also include the Bessel functions of order of zero, unit and second and ten fundamental functions of Φ_{11}, Φ_{13}, Φ_{22}, Φ_{31}, Φ_{33}, Ψ_{11}, Ψ_{13}, Ψ_{22}, Ψ_{31} and Ψ_{33}. The ten fundamental functions are continuous functions of the integral variables $\rho(0\le\rho<\infty)$ and the depth $z(0\le z<\infty)$ except Ψ_{11}, Ψ_{22} and Ψ_{33} have a unit step decrease at *z=d* and that they have no functions of exponential growth. The unit step decrease of Ψ_{11}, Ψ_{22} and Ψ_{33} at *z=d* is due to the presence of the point loads at

$z=d$. In addition, as the integral variable ρ approaches to infinity, the ten fundamental functions quickly vanish to zero by following $e^{-\rho|z-d|}$.

It is noted that the solutions of the plane stresses $\left(\sigma_{xx},\sigma_{xy},\sigma_{yy}\right)$ and the vertical strains $\left(\varepsilon_{xz},\varepsilon_{yz},\varepsilon_{zz}\right)$ due to the point loads F_z and F_x can be easily obtained from the solutions of the vertical stresses $\left(\sigma_{xz},\sigma_{yz},\sigma_{zz}\right)$ and the plane strains $\left(\varepsilon_{xx},\varepsilon_{xy},\varepsilon_{yy}\right)$ by using the constitutive equations. More details of the expressions and mathematical properties of the fundamental solution can be found in Yue [36, 38, 39].

References

[1] Arin K, Erdogan F. Penny-shaped crack in an elastic layer bonded to dissimilar half spaces. *Int J Eng Sci* 1971; 9(2): 213-232.

[2] Lin W, Keer LM. Three-dimensional analysis of cracks in layered transversely isotropic media. *Proceedings of the Royal Society of London*, 1989; A424(1867):307-322.

[3] Kuo CH, Keer LM. Three-dimensional analysis of cracking in a multilayered composite. *J Appl Mech* 1995; 62(2):273-281.

[4] Noda NA, Ohzono R, Chen MC. Analysis of an elliptical crack parallel to a bimaterial interface under tension. *Mech Mater* 2003; 11:1059-1076.

[5] Zhang X, Jeffrey RG. Numerical studies on crack problems in three-layered elastic media using an image method. *Int J Fract* 2006; 139(3-4): 477-493.

[6] Alaimo A, Milazzo A, Orlando C. Application of the 3-D boundary element method to delaminated composite structures. *Eng Fract Mech* 2013; 110: 201-217.

[7] Xiao HT, Yue ZQ. A three-dimensional displacement discontinuity method for crack problems in layered rocks. *Int J Rock Mech Min Sci* 2011; 48(3): 412-420.

[8] Jin Z, Noda N. Crack-tip singular fields in nonhomogeneous materials. ASME *J Appl Mech* 1994; 61:738-740.

[9] Ozturk M, Erdogan F. Axisymmetric crack problem in bonded materials with a graded interfacial region. *Int J Solid Struct* 1996; 33:193-219.

[10] Paulino GH. Fracture of functionally graded materials. *Eng Fract Mech* 2002; 69:1519-1520.

[11] Yue ZQ, Xiao HT, Tham GL. Boundary element analysis of crack problems in functionally graded materials. *Int J Solid Struct* 2003; 40:3273-91.

[12] Birman V, Byrd LW. Modeling and analysis of functionally graded materials and structures. ASME *Appl Mech Rev* 2007; 60(1-6): 195-216.

[13] Rooke DP, Cartwright DJ. *Compendium of stress intensity factors*. Stationery Office, Great Britain, Ministry of Defence, Procurement Executive; 1976.

[14] Tada H, Paris P, Irwin G. The stress analysis of cracks handbook. 3rd edn. New York: ASME; 2000.

[15] Rooke DP, Baratta RJ, Cartwright DJ. Simple methods for determining stress intensity factors. *Eng Fract Mech* 1981; 14(2):397-426.

[16] Rooke DP. An improved compounding method for calculating stress-intensity factors. *Eng Fract Mech* 1986; 23:783-792.

[17] Rooke DP, Tweed J. Stress intensity factors for a crack at the edge of pressurized hole. *Int J Eng Sci* 1980; 18:109-121.

[18] Rooke DP, Rayaprolu DB, Aliabadi MH. Crack-line and edge Green's functions for stress intensity factors of inclined edge cracks. *Fatigue Fract Engng Mater Struct* 1992; 15 (5):441-461.

[19] Cheng AHD, Cheng DT. Heritage and early history of the boundary element method. Eng Anal Bound Elem 2005; 29:268-302.

[20] Aliabadi MH. Boundary element formulations in fracture mechanics. *Appl Mech Rev* 1997; 50(2):83-96.

[21] Hong H, Chen JT. Derivations of integral equations of elasticity. *J Eng Mech* 1988; 114:1028-1044.

[22] Chen JT, Hong HK. Review of dual boundary element methods with emphasis on hypersingular integrals and divergent series. *Appl Mech Rev* 1999; 52:17-32.

[23] Portela A, Aliabadi MH, Rooke DP. Dual boundary element method: efficient implementation for cracked problems. *Int J Numer Meth Eng* 1992; 33:1269-1287.

[24] Mi Y, Aliabadi MH. Dual boundary element method for three-dimensional fracture mechanics analysis. *Eng Anal Bound Elem* 1992;10:161-171.

[25] Portela A, Aliabadi MH, Rooke DP. Dual boundary element incremental analysis of crack propagation. *Comput Struct* 1993; 46(2):237-247.

[26] Mi Y, Aliabadi MH. Three-dimensional crack growth simulation using BEM. *Comput Struct* 1994; 52(5): 871-878.

[27] Wen PH, Aliabadi MH. Dual boundary element method for modelling curved crack paths. *Int J Fract* 2012; 176:127-133.

[28] Li J, Khodaei ZS, Aliabadi MH. Dynamic dual boundary analysis for cracked Mindlin plates. *Int J Solids Struct* 2018; 152:248-260.

[29] Pan E, Amadei B. A 3-D boundary element formulation of anisotropic elasticity with gravity. *Appl Math Model* 1996; 20:114-120.

[30] Pan E. A general boundary element analysis of 2D linear elastic fracture mechanics. *Int J Fract* 1997; 88:41-59.

[31] Pan E, Yuan FG. Boundary element analysis of three-dimensional cracks in anisotropic solids. *Int J Numer Meth Eng* 2000; 48:211-237.

[32] Cisilino AP, Aliabadi MH. Three-dimensional BEM analysis for fatigue crack growth in welded components. *Int J Pres Piping* 1997; 70:135-144.

[33] Cisilino AP, Otegui JL, Aliabadi MH. A three-dimensional dual boundary element formulation for the elastoplastic analysis of cracked bodies. *Int J Numer Meth Eng* 1998; 42:237-256.

[34] Yue ZQ, Xiao HT, Pan E. Stress intensity factors of square crack inclined to interface of transversely isotropic bi-material. *Eng Anal Bound Elem* 2007; 31(1): 50-65.

[35] Dong CY, Yang X, Pan E. Analysis of cracked transversely isotropic and inhomogeneous solids by a special BIE formulation. *Eng Anal Bound Elem* 2011; 35:200-206.

[36] Yue ZQ. On generalized Kelvin solutions in a multilayered elastic medium. *J Elast* 1995; 40:1-43.

[37] Selvadurai APS. On Boussinesq's problem for a cracked halfspace. *J Eng Math* 2017, 107(1): 269-282.

[38] Yue ZQ. Yue's solution of classical elasticity in n-layered solids: Part 1, mathematical formulation. *Front Struct Civ Eng* 2015; 9:215-249.

[39] Yue ZQ. Yue's solution of classical elasticity in n-layered solids: Part 2, mathematical

verification. *Front Struct Civ Eng* 2015; 9:250-285.

[40] Xiao HT, Yue ZQ. *Fracture mechanics in layered and graded materials: analysis using boundary element methods*, Berlin: De Gruyter and Beijing: Higher Education Press, 2014.

[41] Xiao S, Yue ZQ, Xiao HT. Boundary element analysis of elastic fields in non-horizontally layered halfspace whose horizontal boundary subject to tractions. *Eng Anal Bound Elem* 2018; 95:105-123.

[42] Beer G, Smith I, Duenser C. *The boundary element method with programming for engineering and scientists*. New York: Springer Wien; 2008.

[43] Kutt HR. *Quadrature formulae for finite-part integrals*. Special Report WISK 178, National Research Institute for Mathematical Sciences, Pretoria, 1975.

[44] Kutt HR. *On the numerical evaluation of finite-part integrals involving an algebraic singularity*. Special Report WISK 179, National Research Institute for Mathematical Sciences, Pretoria, 1975.

[45] Weaver J. Three-dimensional crack analysis. *Int J Solids Struct* 1977; 13: 321-330.

Table 1 The maximum SIF values under the action of a compressive stress on the crack surface

Case no	SIFs	*h/a*			
		0.5	1	1.5	3
1	*KI*	1.34204	0.99550	0.83971	0.77194
	KII	0.31149	0.09480	0.02725	0.00259
	KIII	0.10754	0.04580	0.01585	0.00192
2	*KI*	1.45188	1.04010	0.86293	0.77803
	KII	0.25117	0.05344	0.01743	0.00146
	KIII	0.08760	0.02654	0.01032	0.00120

Table 2 The maximum SIF values under the action of a tensile stress on the external boundary surface

Case no	SIFs	*h/a*			
		0.2	0.3	0.4	0.5
1	*KI*	3.37182	2.04106	1.46441	1.13244
	KII	1.52567	0.87319	0.57433	0.40855
	KIII	0.32154	0.22673	0.17545	0.14083
2	*KI*	3.51686	2.08922	1.49037	1.14583
	KII	1.37491	0.79612	0.53013	0.38241
	KIII	0.29076	0.21739	0.17287	0.14047

Table 3 The SIF values of a penny-shaped crack located at the interface between a graded layer and a homogeneous halfspace

h/a	$\alpha=-1$		$\alpha=-0.5$		$\alpha=0.5$		$\alpha=1$	
	KI	*KII*	*KI*	*KII*	*KI*	*KII*	*KI*	*KII*
0.5	1.77069	0.49528	1.72732	0.43292	1.63316	0.30989	1.58307	0.24995
0.6	1.64684	0.38607	1.59360	0.31937	1.48176	0.19124	1.42429	0.13096
0.7	1.55859	0.31538	1.49755	0.24598	1.37246	0.11638	1.30998	0.05767
0.8	1.49717	0.26817	1.42628	0.19711	1.29067	0.06779	1.22303	0.01183
0.9	1.44820	0.23641	1.37213	0.16379	1.22765	0.03540	1.15759	-0.01806
1.0	1.41104	0.21466	1.33027	0.14067	1.17793	0.01329	1.10586	-0.03769
1.1	1.38264	0.19979	1.29752	0.12443	1.13792	-0.00215	1.06411	-0.05084
1.2	1.36096	0.18977	1.27172	0.11293	1.10522	-0.01314	1.02983	-0.05981
1.3	1.34455	0.18323	1.25174	0.10460	1.07788	-0.02096	1.00126	-0.06607
1.4	1.33235	0.17919	1.23537	0.09882	1.05526	-0.02689	0.97715	-0.07051
1.5	1.32351	0.17694	1.22237	0.09475	1.03609	-0.03137	0.95658	-0.07372

Table 4 The modes I and II SIF values of an elliptical crack located at the interface between a graded layer and a homogeneous halfspace (β=90^{o})

h/a	α=−1		α=−0.5		α=0.5		α=1	
	KI	*KII*	*KI*	*KII*	*KI*	*KII*	*KI*	*KII*
0.5	1.255	0.15269	1.21781	0.12011	1.14348	0.05849	1.10666	0.02983
0.6	1.17413	0.11798	1.13216	0.08456	1.04969	0.02339	1.00967	-0.00392
0.7	1.11968	0.09908	1.07335	0.06494	0.98371	0.00438	0.94105	-0.02163
0.8	1.08217	0.08945	1.03178	0.0538	0.93563	-0.00639	0.89087	-0.03175
0.9	1.05619	0.0877	1.00188	0.04737	0.89969	-0.01275	0.85292	-0.03715
1.0	1.03809	0.08678	0.98009	0.04367	0.87227	-0.01668	0.82372	-0.04035
1.1	1.02554	0.08559	0.96408	0.0416	0.85094	-0.01923	0.80079	-0.04239
1.2	1.01695	0.08389	0.95225	0.04055	0.83408	-0.02099	0.78243	-0.04381
1.3	1.01123	0.08351	0.9435	0.04022	0.82056	-0.02233	0.76748	-0.0449
1.4	1.0076	0.08221	0.93698	0.04021	0.80949	-0.02332	0.75509	-0.04585
1.5	1.00553	0.08201	0.93217	0.0405	0.80033	-0.02416	0.74456	-0.04673

Table 5 The mode III SIF values of an elliptical crack located at the interface between a graded layer and a homogeneous halfspace

h/a	$\alpha=-1$		$\alpha=-0.5$		$\alpha=0.5$		$\alpha=1$	
	$\beta=39.64^{o}$	$\beta=63.43^{o}$	$\beta=39.64^{o}$	$\beta=63.43^{o}$	$\beta=39.64^{o}$	$\beta=63.43^{o}$	$\beta=39.64^{o}$	$\beta=63.43^{o}$
0.5	0.03914	0.05258	0.03491	0.04738	0.02607	0.03626	0.02153	0.03044
0.6	0.03149	0.04147	0.02665	0.03542	0.01679	0.02292	0.01188	0.01664
0.7	0.02628	0.03394	0.02099	0.02729	0.0105	0.01402	0.00547	0.00763
0.8	0.0227	0.02879	0.01706	0.02172	0.00621	0.00806	0.00119	0.00177
0.9	0.02021	0.02528	0.01431	0.01787	0.00325	0.00403	-0.00166	-0.00208
1.0	0.01847	0.02285	0.01236	0.01516	0.00119	0.00127	-0.00356	-0.00459
1.1	0.01726	0.02115	0.01096	0.01324	-0.00026	-0.00063	-0.00484	-0.00622
1.2	0.01642	0.01995	0.00995	0.01186	-0.0013	-0.00196	-0.00568	-0.00726
1.3	0.01585	0.01911	0.00922	0.01087	-0.00203	-0.00289	-0.00624	-0.00791
1.4	0.01547	0.01851	0.00869	0.01013	-0.00256	-0.00355	-0.0066	-0.00831
1.5	0.01523	0.01811	0.00831	0.00959	-0.00295	-0.00401	-0.00683	-0.00854

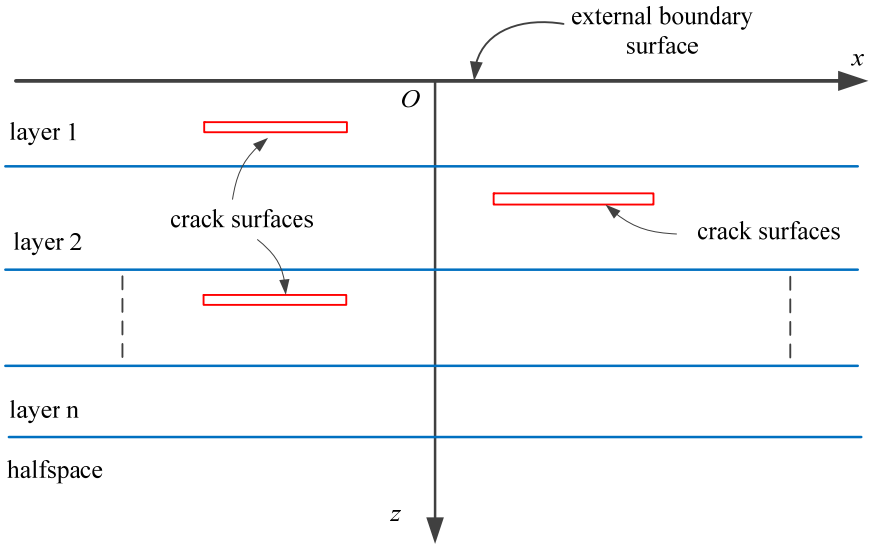

Fig. 1 Three-dimensional cracks in a horizontally layered halfspace

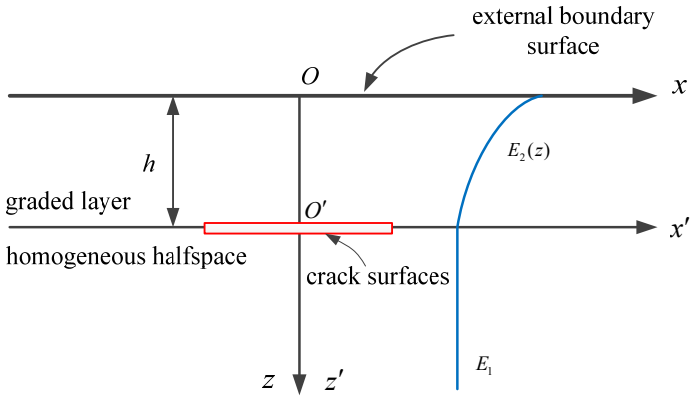

Fig. 2 A three-dimensional crack located at the interface between a graded layer and a homogeneous halfspace

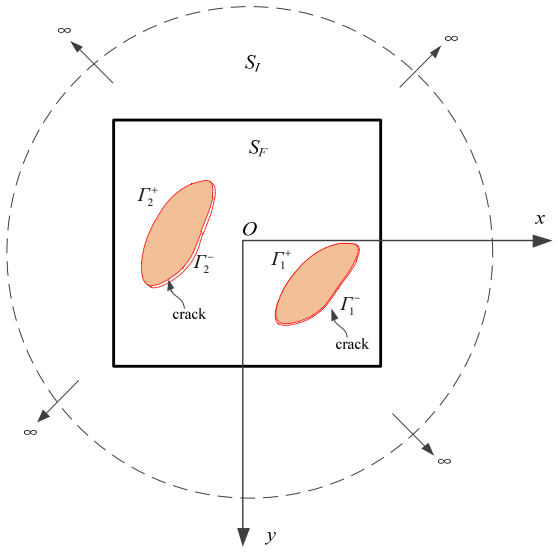

Fig. 3 Subdivision of boundary and crack surfaces for a cracked and layered halfspace; Γ_i^+ and Γ_i^- are the two sides of crack surfaces Γ_i; $S\left(=S_F+S_I\right)$ is the external boundary surface.

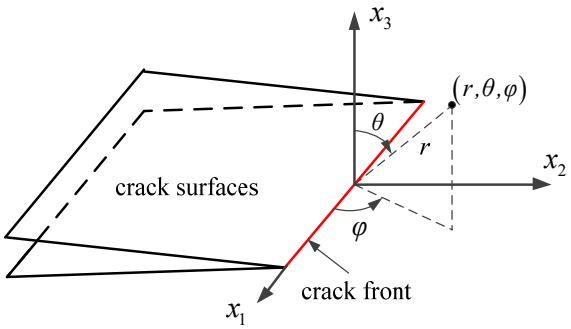

Fig. 4 Local coordinate systems $\left(x_1,x_2,x_3\right)$ and $\left(r,\theta,\varphi\right)$ located at the crack front

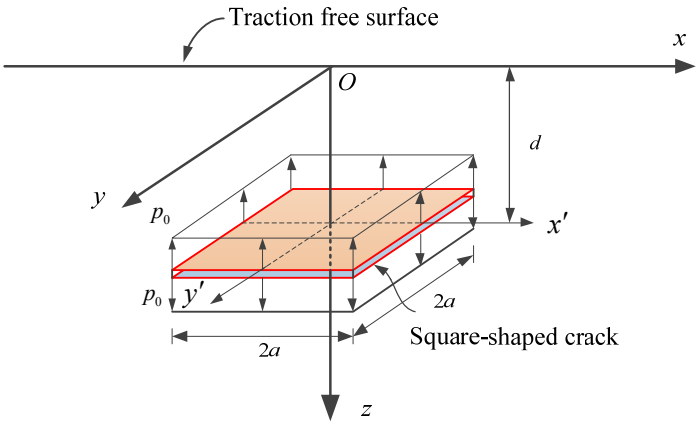

Fig. 5 A square-shaped crack in a homogeneous halfspace parallel to the boundary surface and subject to a uniform compressive stress on the crack surface

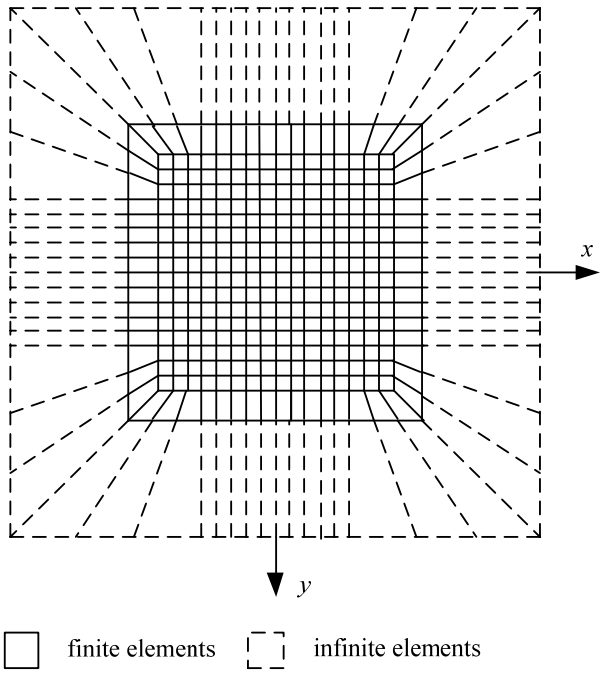

Fig. 6 Discretization of a traction free surface with 230 finite elements and 64 infinite elements

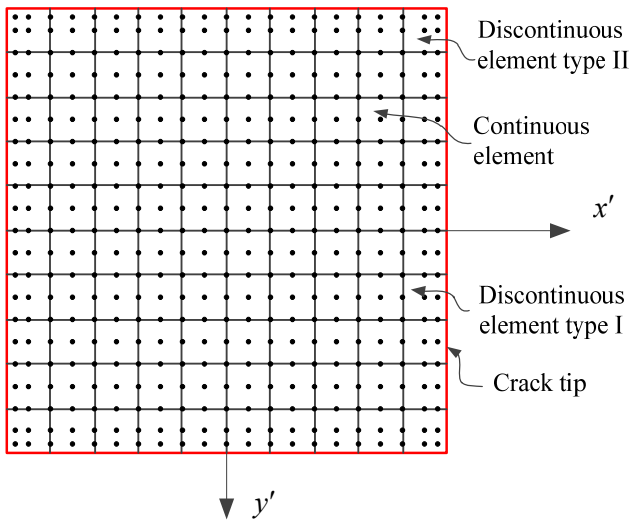

Fig. 7 Discretization of a square-shaped crack with 100 nine-node quadrilateral elements

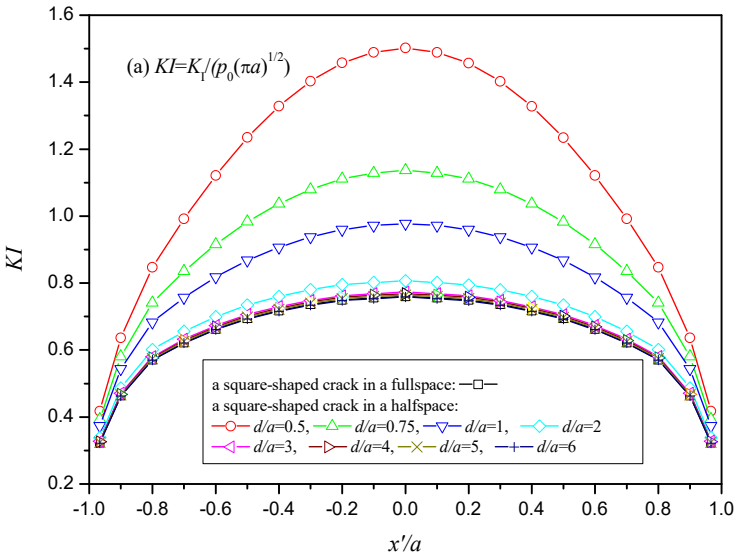

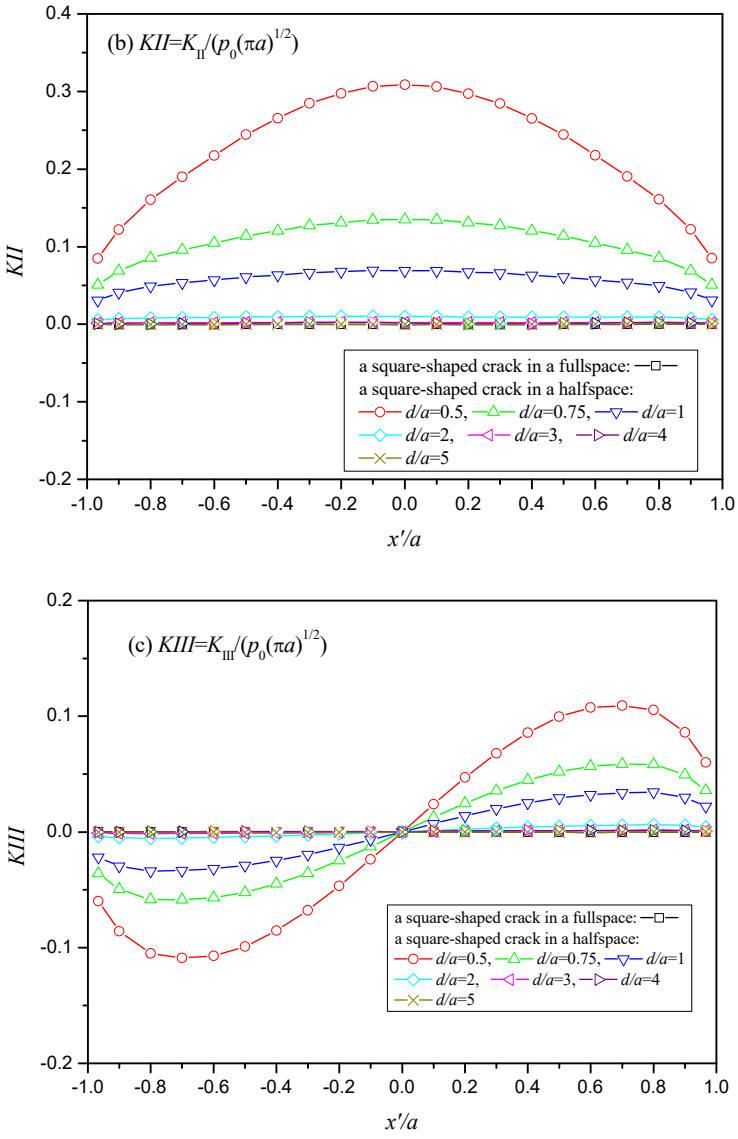

Fig. 8 The normalized SIFs *KI*, *KII* and *KIII* of a square-shaped crack in a homogeneous halfspace with the depth *d*

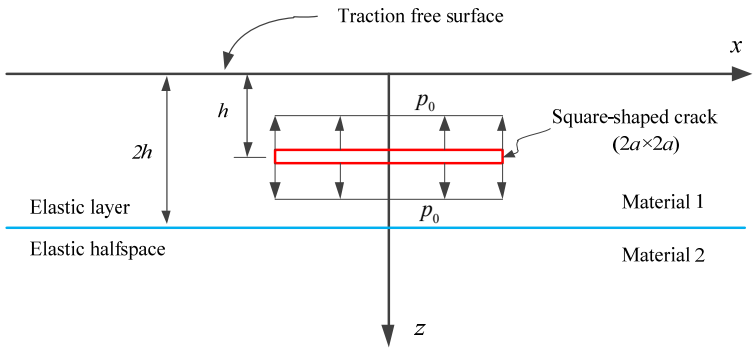

Fig. 9 A square-shaped crack in a horizontally layered bi-material halfspace under a uniform compressive stress

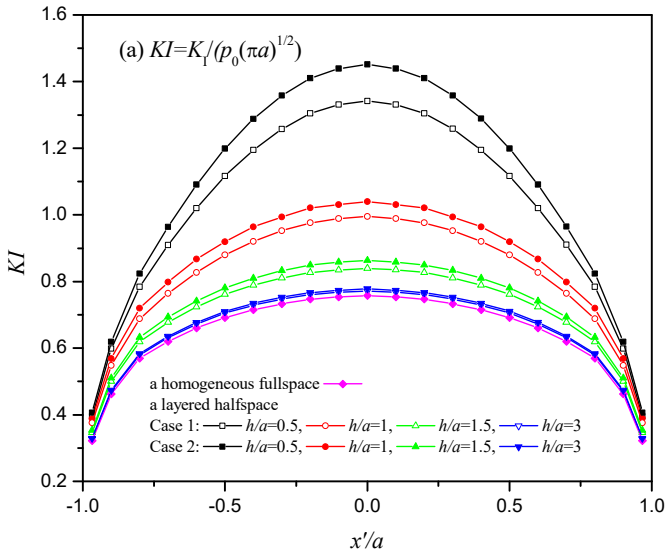

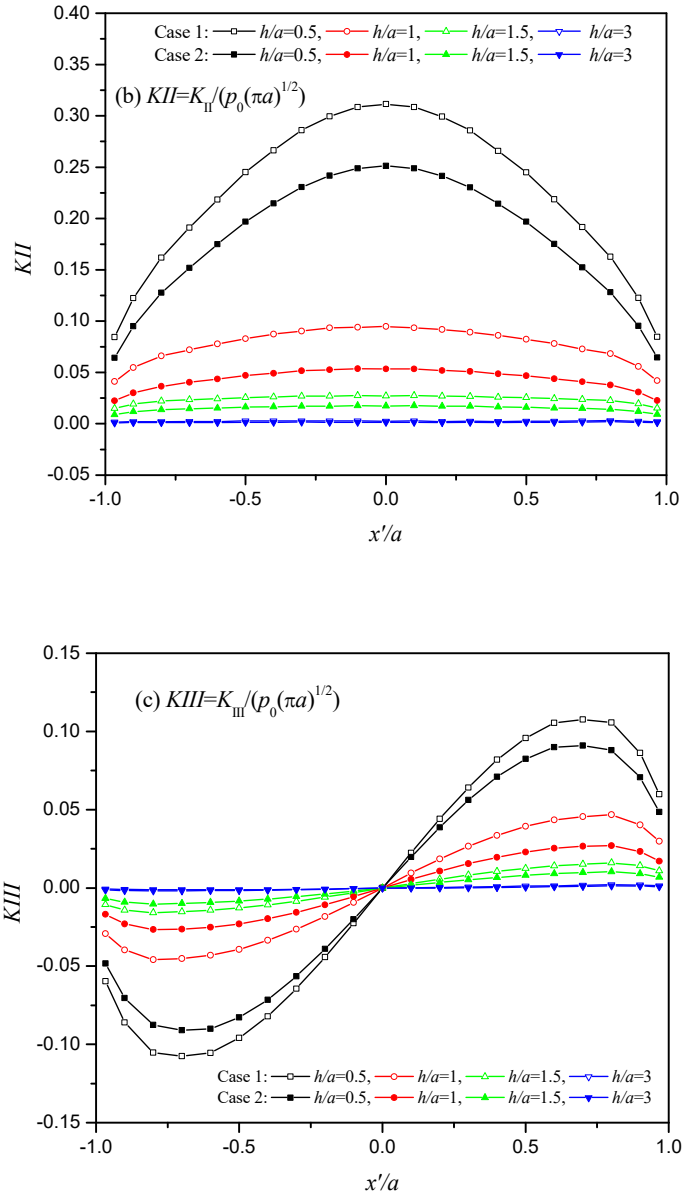

Fig. 10 The normalized SIFs *KI*, *KII* and *KIII* of a square-shaped crack under a uniform compressive stress

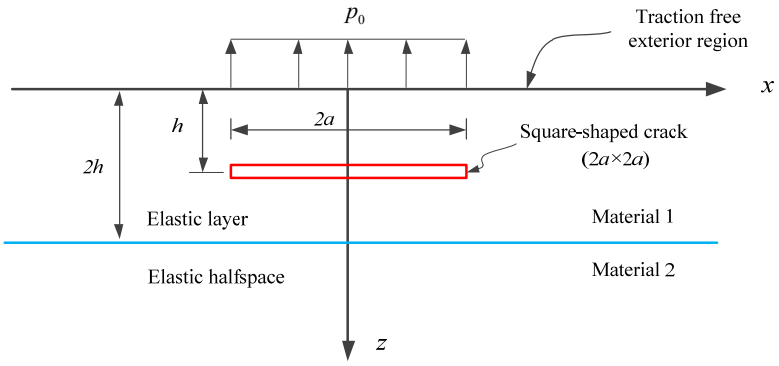

Fig. 11 A square-shaped crack in a horizontally layered bi-material halfspace under a uniform tensile stress on the external boundary surface

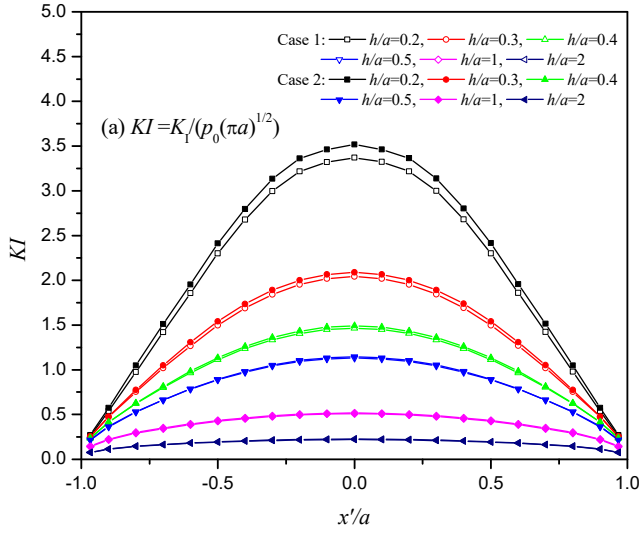

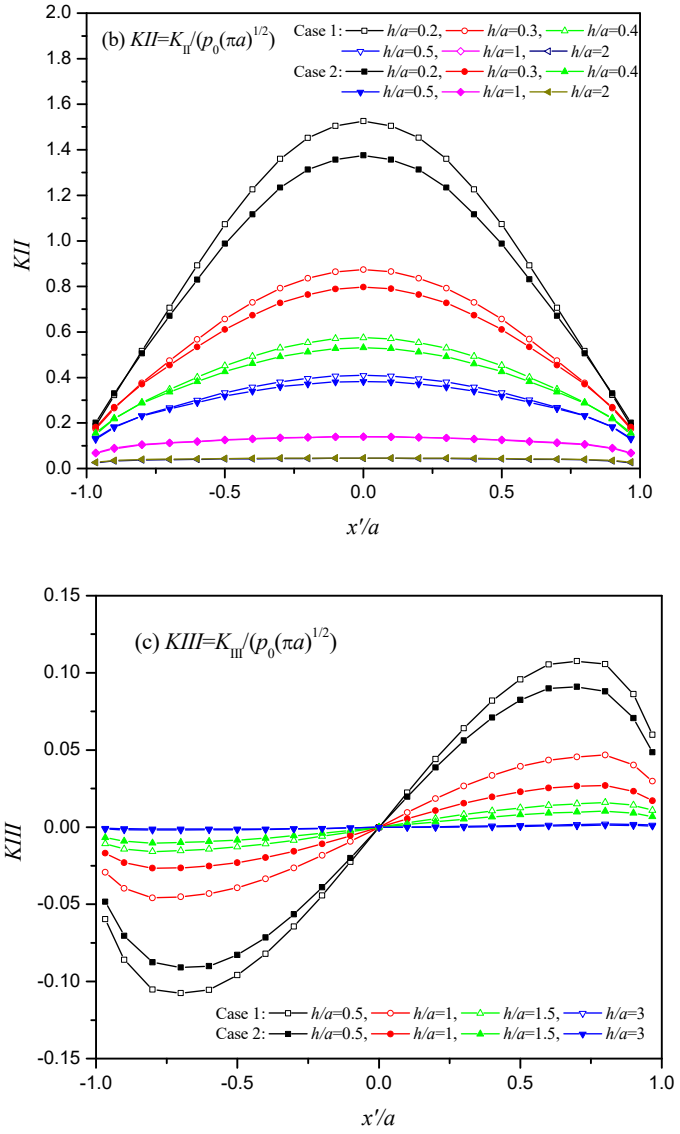

Fig. 12 The normalized SIFs *KI*, *KII* and *KIII* of a square-shaped crack under a uniform tensile stress on the external boundary surface

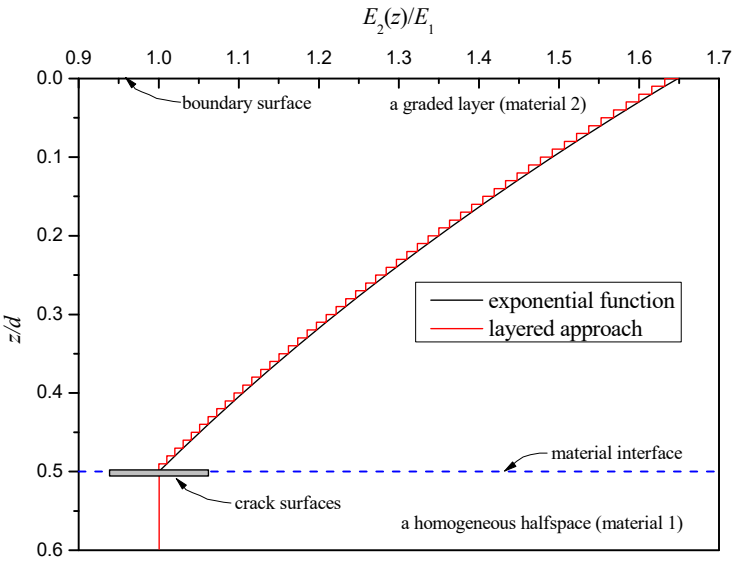

Fig. 13 Approximation of the continuous depth variation of the elastic modulus by a layered system of 50 piece-wisely homogeneous layers for α=1 and $h/a=0.5$

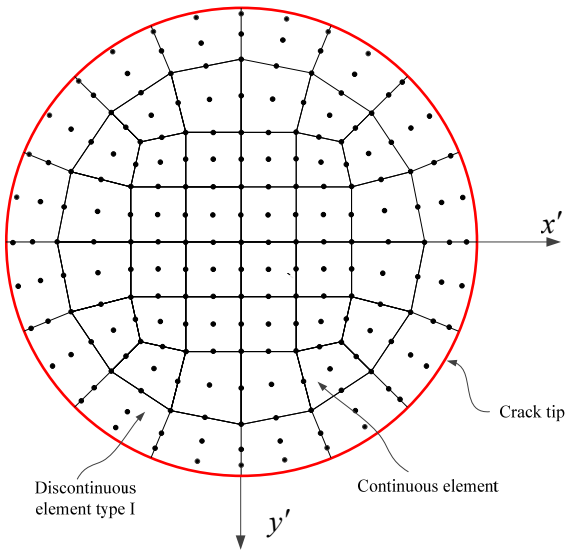

Fig. 14 Discretization of a penny-shaped crack with 64 nine-node quadrilateral elements

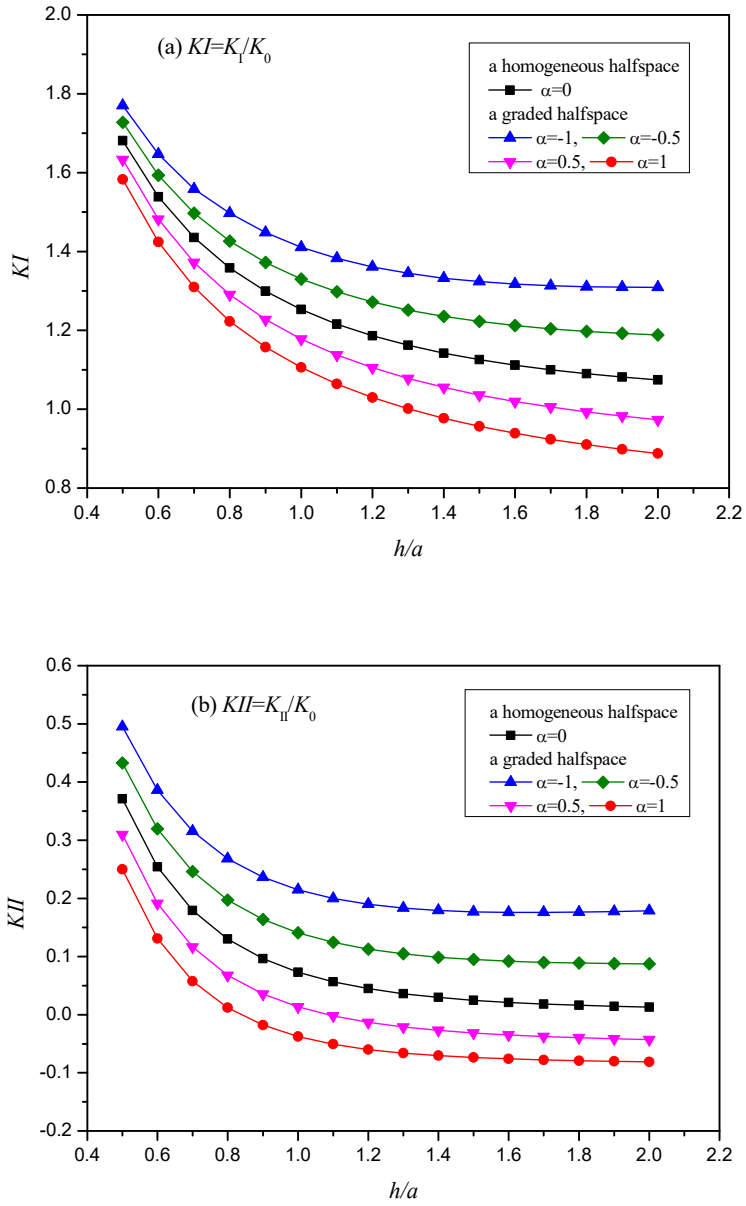

Fig. 15 The normalized SIFs *KI* and *KII* for the penny-shaped crack located at the interface between a graded layer and a homogeneous halfspace

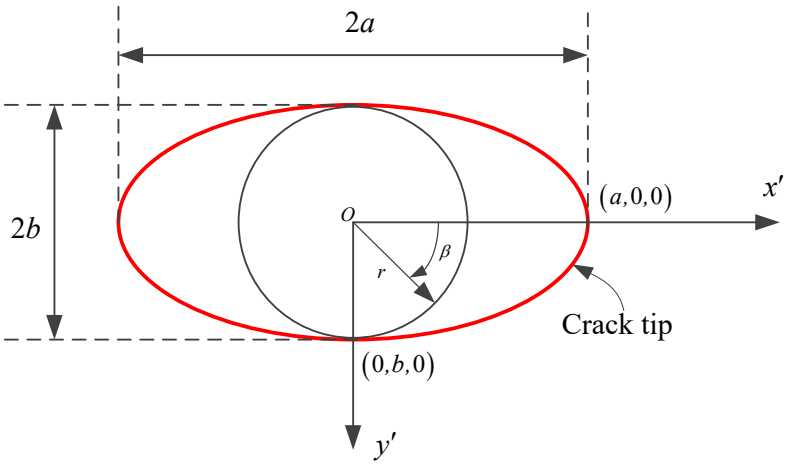

Fig. 16 An elliptical crack located at the interface between a graded layer and a homogeneous halfspace

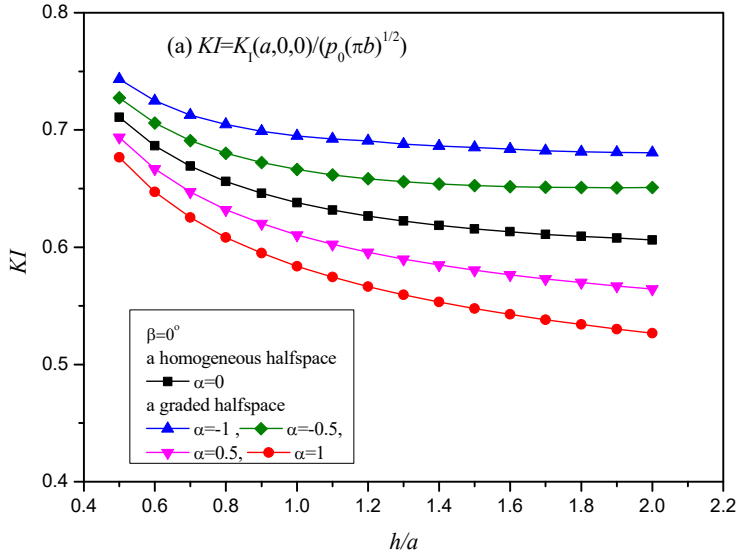

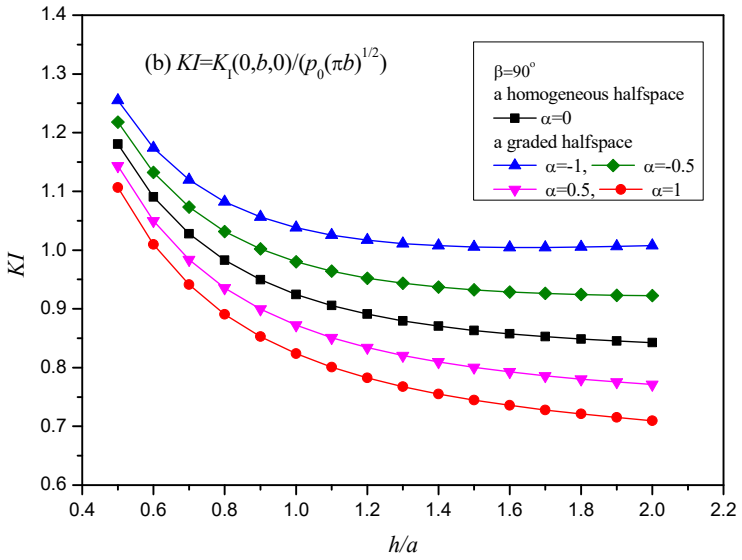

Fig. 17 The normalized SIF *KI* for the elliptical crack located at the interface between a graded layer and a homogeneous halfspace (β=0°,90°)

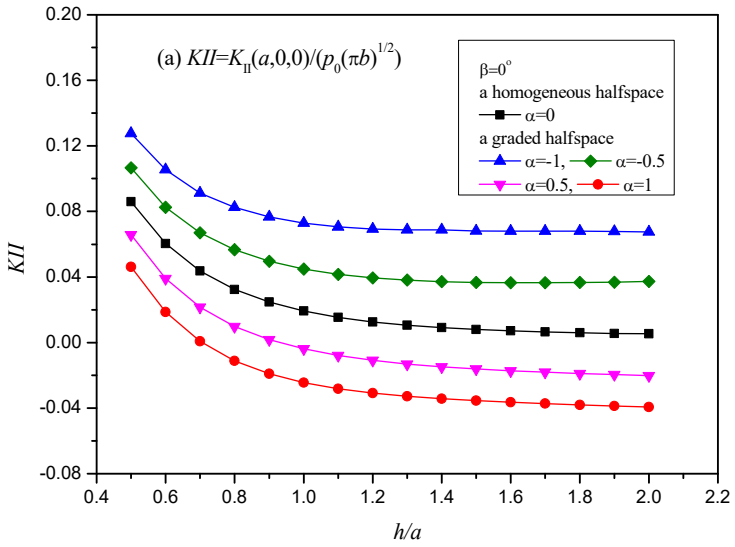

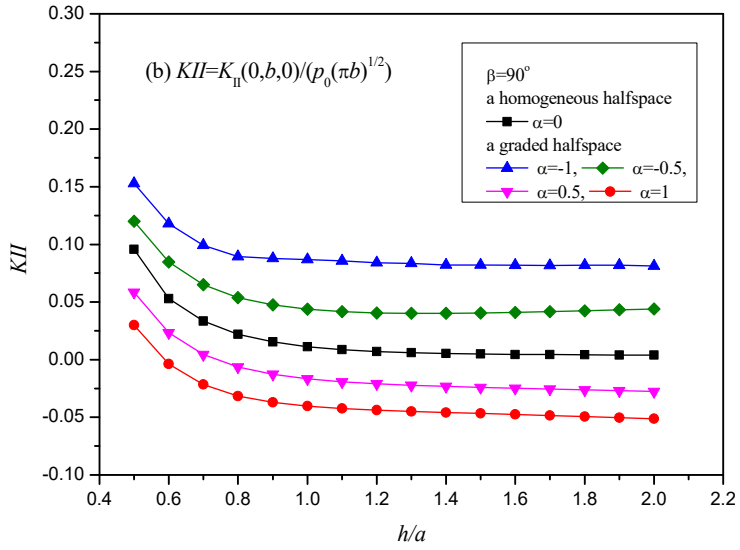

Fig. 18 The normalized SIF *KII* for the elliptical crack located at the interface between a graded layer and a homogeneous halfspace (β=0°,90°)

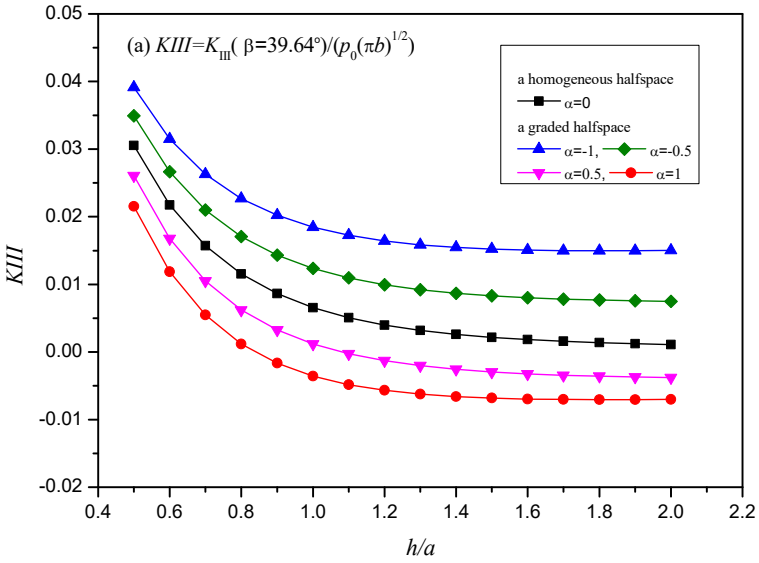

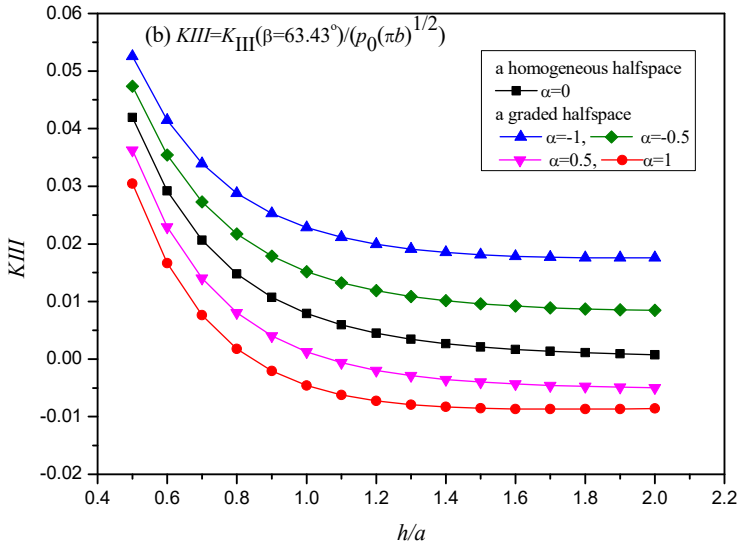

Fig. 19 The normalized SIF *KIII* for the elliptical crack located at the interface between a graded layer and a homogeneous halfspace (β=39.64°,63.43°)